Supplement Material

High-frequency monitoring of SO_2 plumes from small volcanic eruptions using a synergy of GEO and LEO satellites: A case study of the 2024 Kanlaon eruption

Shangyi Liu[1], Yingjun Zheng[1], Mengya Sheng[1], Lu Lee[2], Chengli Qi[2], Feng Lu[2], Bruno Franco[3], Lieven Clarisse[3], Cathy Clerbaux[3,4], Nicolas Theys[5], Jhoon Kim[6,7], Zhao-Cheng Zeng[1,*]

[1] School of Earth and Space Sciences, Peking University, Beijing, China
[2] Innovation Center for FengYun Meteorological Satellite, Key Laboratory of Radiometric Calibration and Validation for Environmental Satellites, National Satellite Meteorological Center, China Meteorological Administration, Beijing 100081, China
[3] Université libre de Bruxelles (ULB), BLU-ULB research Center, Spectroscopy, Quantum Chemistry and Atmospheric Remote Sensing (SQUARES), Brussels, Belgium
[4] LATMOS/IPSL, Sorbonne Université, UVSQ, CNRS, Paris, France
[5] Royal Belgian Institute for Space Aeronomy (BIRA-IASB), Brussels, Belgium
[6] Department of Atmospheric Science, Yonsei University, Seoul, Korea
[7] Max Planck Institute for Meteorology, Hamburg, Germany

Correspondence to: Zhao-Cheng Zeng (zczeng@pku.edu.cn)

Address: No.5 Yiheyuan Road, Haidian District, Beijing 100871, P. R. China

Contents of this file

Text S1: The forward model

In the forward simulations, the top-of-atmosphere radiance received by the sensor is modeled as the summation of four radiative components: (a) surface thermal emission, (b) upwelling atmospheric emission, (c) downwelling atmospheric radiance reflected by the surface, and (d) reflected solar radiation. Molecular and aerosol scattering are considered negligible in the thermal infrared region and are thus excluded. For numerical implementation, the atmosphere is discretized into a fixed 34-layer pressure grid ranging from 1000 hPa to 1 hPa (see Table S1). The vertical resolution is approximately 1 km below 25 km and increases to 2.5 km above this altitude (based on the USSA model). The thickness of the bottom layer is dynamically adjusted based on the actual surface pressure. More detailed description described in **Zeng et al. (2023a)**.

Input parameters for the forward model are derived from multiple high-resolution datasets. Profiles for atmospheric temperature, water vapor, and O_3, along with surface skin temperature and surface pressure, are sourced from the European Centre for Medium-Range Weather Forecasts (ECMWF) Reanalysis v5 (ERA5) **(Hersbach et al., 2020)**. CO_2 profiles are obtained from the ECMWF CAMS model. The prior vertical distribution of SO_2 and other interfering species follow the Line-By-Line Radiative Transfer Model (LBLRTM) standard atmospheric backgrounds. Surface emissivity is derived from the University of Wisconsin-Madison Global Infrared Land Surface Emissivity database **(Seemann et al., 2008)**. To optimize computational efficiency, gas absorption coefficients were pre-calculated using the LBLRTM v12.11 to construct look-up tables (LUTs). This spectroscopic database, based on HITRAN **(Clough et al., 2005; Rothman et al., 2013)**, encompasses 50 pressure levels and 15 temperature levels ranging from 180 K to 320 K at 10 K intervals.

Reference

Clough, S. A., Shephard, M. W., Mlawer, E. J., Delamere, J. S., Iacono, M. J., Cady-Pereira, K., Boukabara, S., & Brown, P. D. (2005). Atmospheric radiative transfer modeling: A summary of the AER codes. Journal of Quantitative Spectroscopy and Radiative Transfer, 91(2), 233–244. https://doi.org/10.1016/j.jqsrt.2004.05.058

Hersbach, H., Bell, B., Berrisford, P., Hirahara, S., Horányi, A., Muñoz-Sabater, J., Nicolas, J., Peubey, C., Radu, R., Schepers, D., Simmons, A., Soci, C., Abdalla, S., Abellan, X., Balsamo, G., Bechtold, P., Biavati, G., Bidlot, J., Bonavita, M., … Thépaut, J. (2020). The ERA5 global reanalysis. Quarterly Journal of the Royal Meteorological Society, 146(730), 1999–2049. https://doi.org/10.1002/qj.3803

Rothman, L. S., Gordon, I. E., Babikov, Y., Barbe, A., Chris Benner, D., Bernath, P. F., Birk, M., Bizzocchi, L., Boudon, V., Brown, L. R., Campargue, A., Chance, K., Cohen, E. A., Coudert, L. H., Devi, V. M., Drouin, B. J., Fayt, A., Flaud, J.-M., Gamache, R. R., … Wagner, G. (2013). The HITRAN2012 molecular spectroscopic database. Journal of Quantitative Spectroscopy and Radiative Transfer, 130, 4–50. https://doi.org/10.1016/j.jqsrt.2013.07.002

Seemann, S. W., Borbas, E. E., Knuteson, R. O., Stephenson, G. R., & Huang, H.-L. (2008). Development of a global infrared land surface emissivity database for application to clear sky sounding retrievals from multispectral satellite radiance measurements. Journal of Applied Meteorology and Climatology, 47(1), 108–123. https://doi.org/10.1175/2007JAMC1590.1

Zeng, Z.-C., Lee, L., & Qi, C. (2023a). Diurnal carbon monoxide observed from a geostationary infrared hyperspectral sounder: First result from GIIRS on board FengYun-4B. Atmospheric Measurement Techniques, 16(12), 3059–3083. https://doi.org/10.5194/amt-16-3059-2023

Table S1. Pressure-level definitions in our forward model vertical grid

Layer idex	Top Pressure (hPa)	Layer idex	Top Pressure
1	1013	19	75.65
2	898.8	20	64.67
3	795.0	21	55.29
4	701.2	22	47.29
5	616.6	23	40.47
6	540.5	24	34.67
7	472.2	25	29.72
8	411.1	26	25.49
9	356.5	27	17.43
10	308.0	28	11.97
11	265.0	29	8.01
12	227.0	30	5.75
13	194.0	31	4.15
14	165.8	32	2.87
15	141.7	33	2.06
16	121.1	34	1.49
17	103.5	35	1.09
18	88.5		

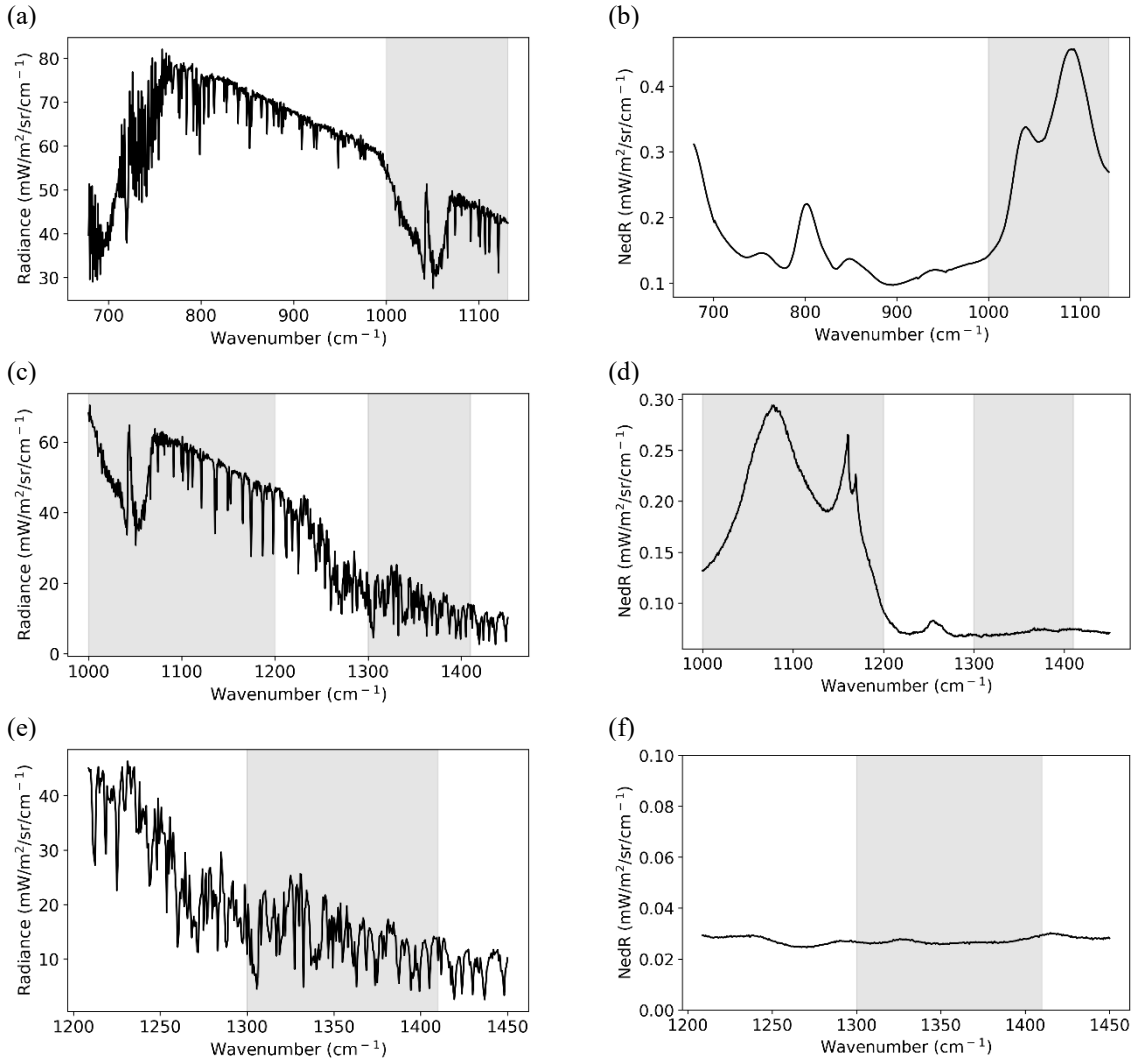

Figure S1. Spectral characteristics and noise performance of the hyperspectral infrared sounders used in this study. (a, c, e) Mean observed long-wave infrared spectra from FY-4B/GIIRS, FY-3E/3F HIRAS, and JPSS-1/2 CrIS, respectively, collected on June 2, 2024, over the potential volcanic plume region. (b, d, f) Corresponding on-orbit Noise Equivalent differential Radiance (NEdR) for each sensor. The gray shaded regions indicate the spectral windows selected for the physical retrieval algorithm: *v*1 (1000–1200 cm^{-1}) and *v*3 (1300–1410 cm^{-1}).

(a)

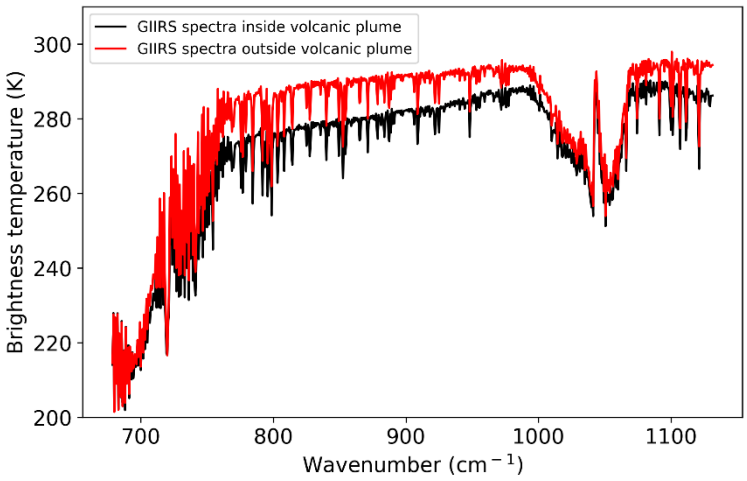

(b)

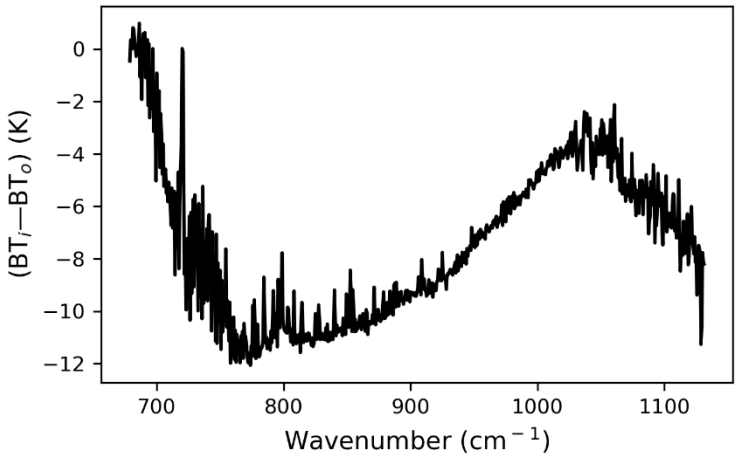

Figure S2. (a) FY-4B/GIIRS LWIR spectra (in brightness temperature (BT)) recorded on 3 June 2024 (16.3 UTC). The black curve denotes the spectrum measured within the volcanic plume, and the spectrum in red is taken from a nearby pixel outside the plume. (b) The BT difference ((ΔBT = BT_in − BT_out) between the two spectra, showing the spectral signatures of ice crystal, volcanic ash and SO_2 in the v1 band.

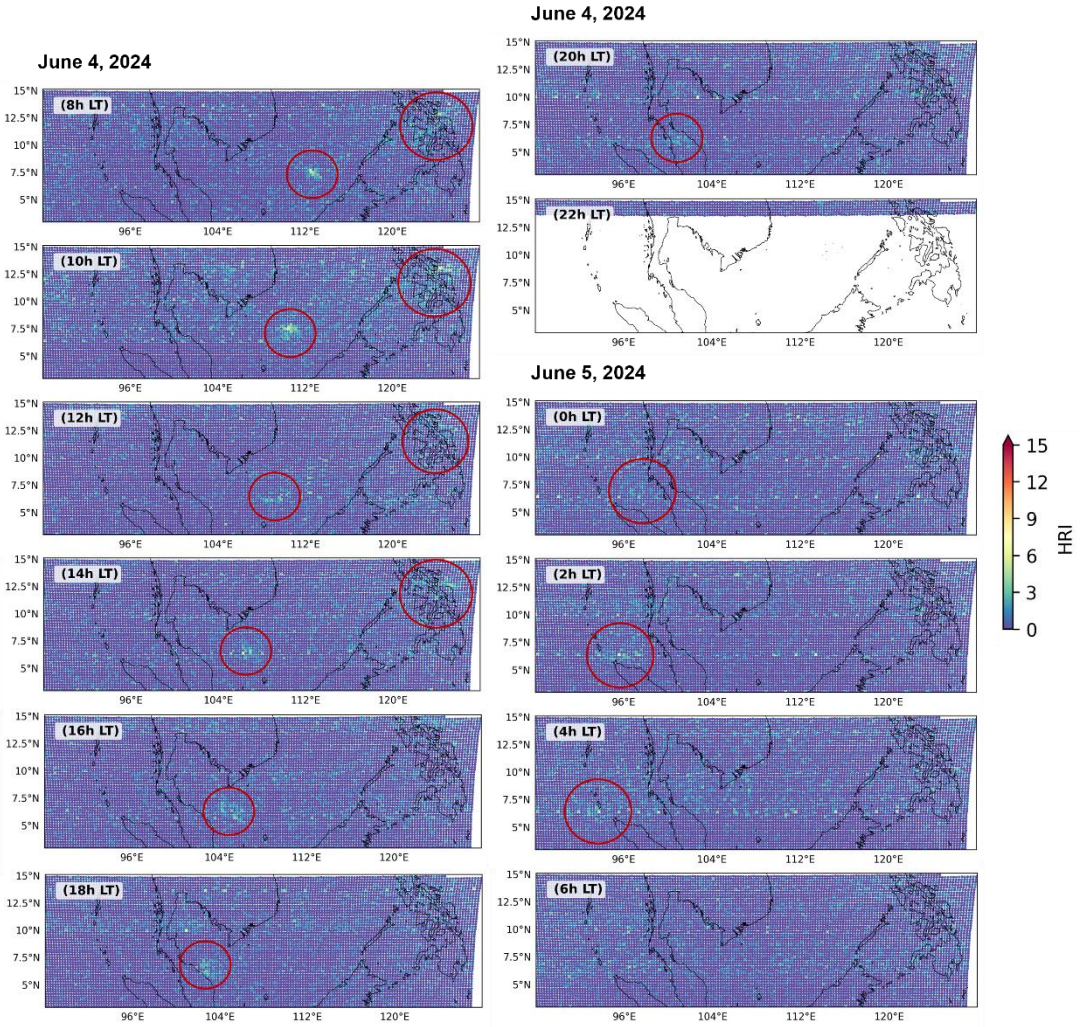

Figure S3. Spatial distribution of the SO_2 HRI derived from FY-4B/GIIRS observations subsequent to the period shown in Figure 5. The panels cover the remaining observation hours on June 4 and 0h–6h LT on June 5, 2024. Red circles indicate areas with high HRI values, tracking the core of the volcanic plume.

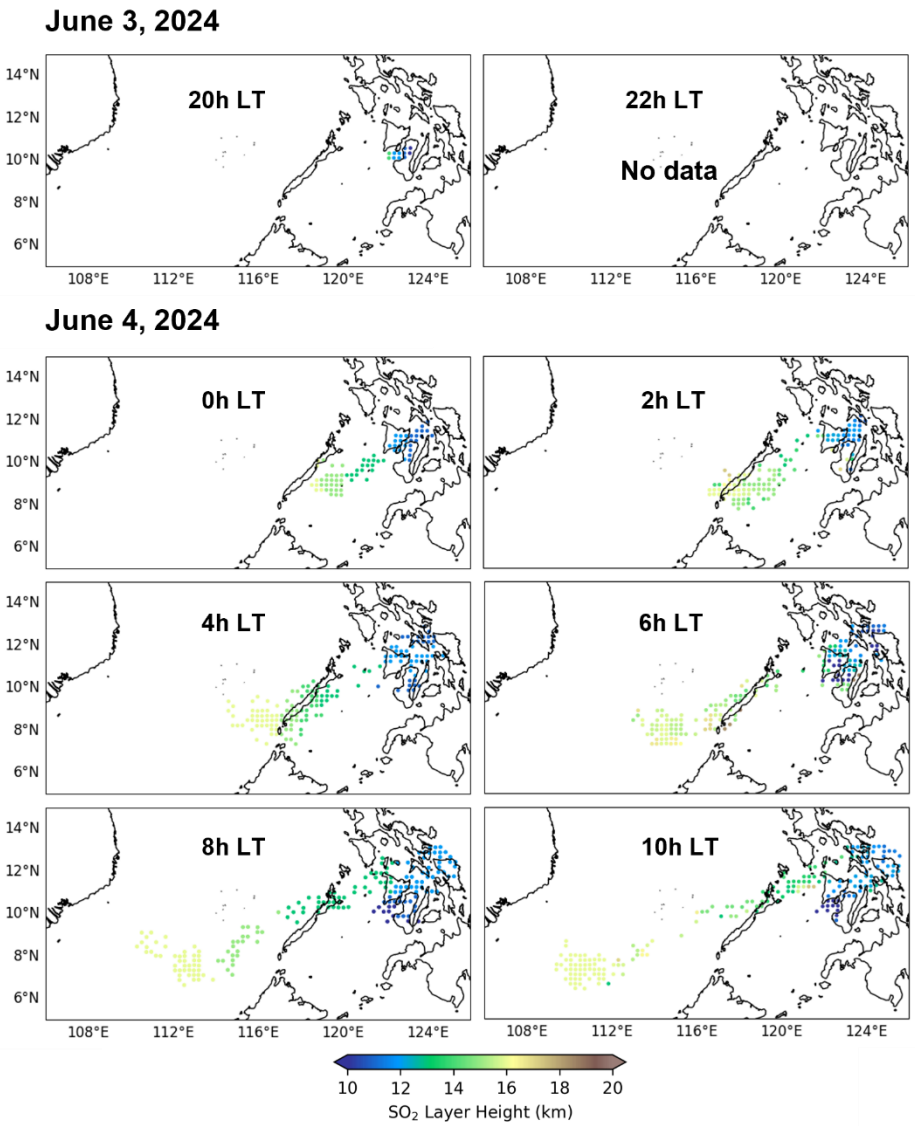

Figure S4. Spatial distribution of the SO_2 plume layer height for FY-4B/GIIRS SO_2 total column retrievals. The plume height information is derived from synergistic observations by FY-3E/F HIRAS and JPSS-1/2 CrIS.

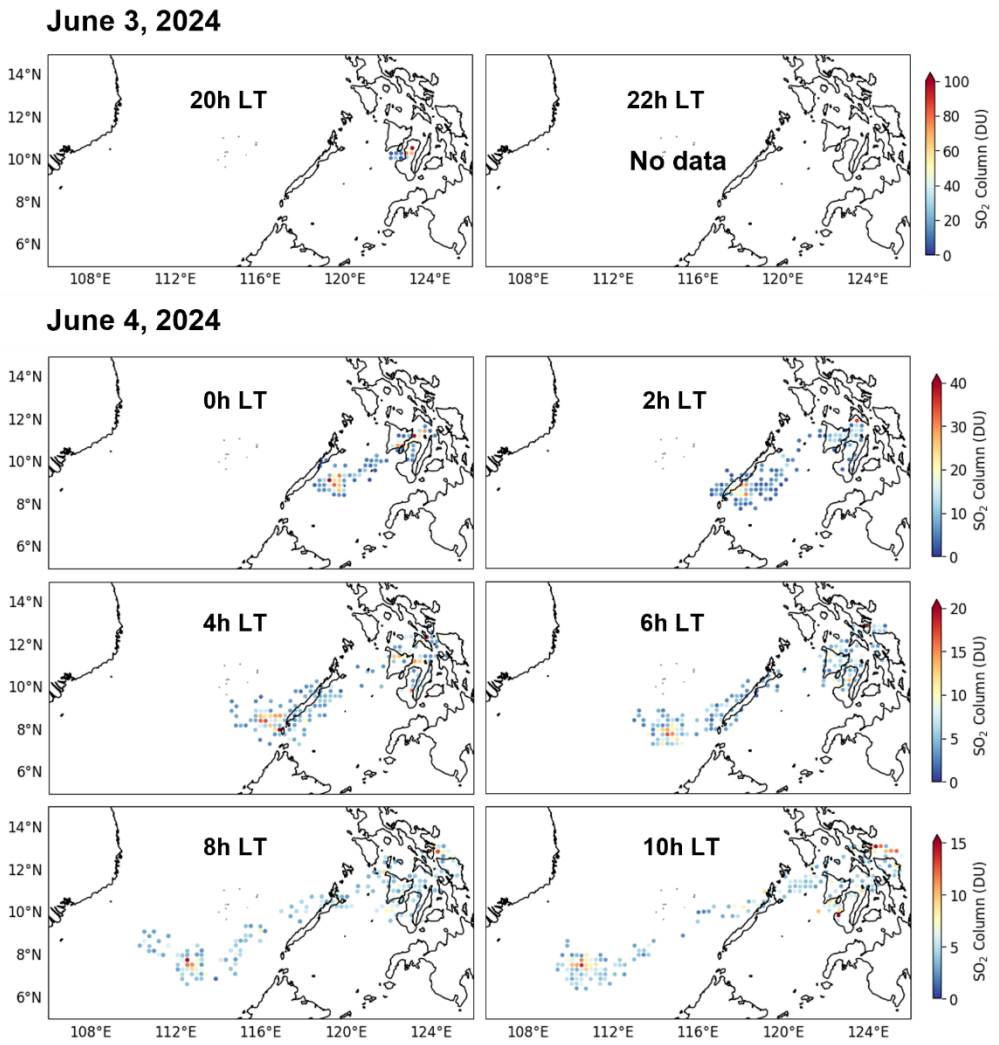

Figure S5. Spatial distribution of SO_2 total column retrieved from FY-4B/GIIRS. The panels correspond to the observations shown in Fig. 5 but within independent color scales.

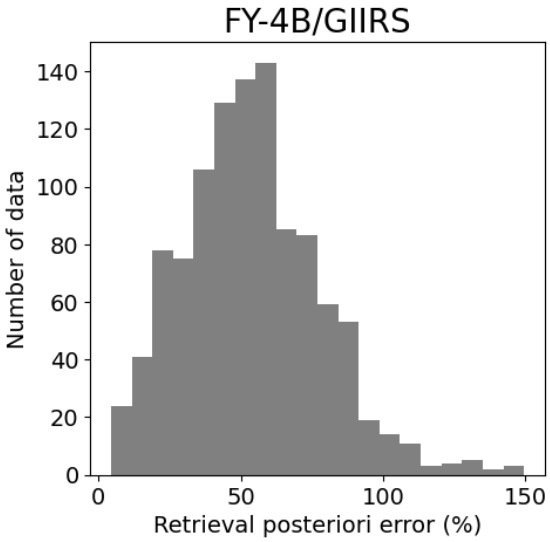

Figure S6. Estimated posterior retrieval error for FY-4B/GIIRS SO_2 total column. The histogram illustrates the statistical spread of retrieval uncertainties, with a mean estimated error of 53.7 ± 24.1%.

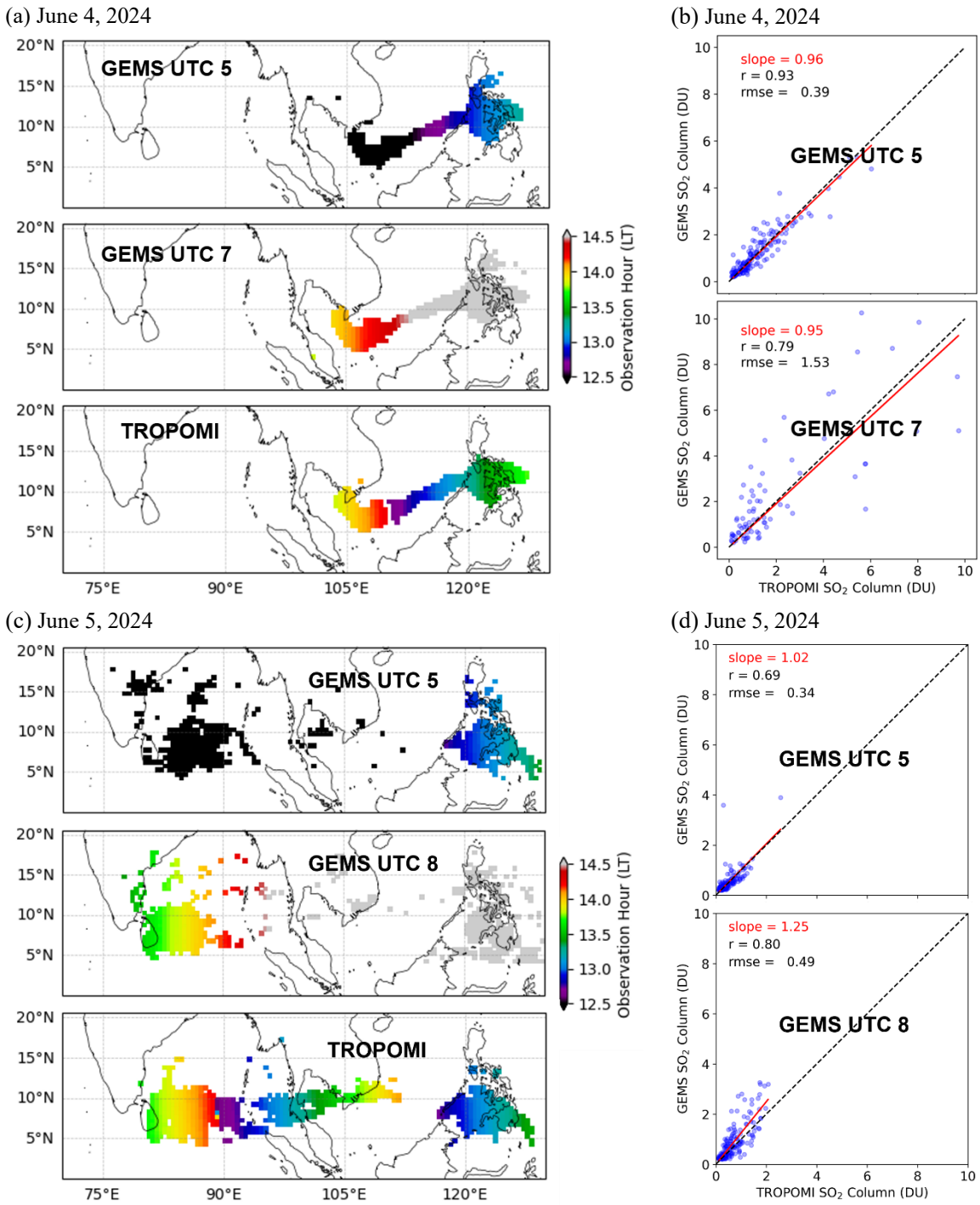

Figure S7. Bias correction of GEMS SO_2 results based on TROPOMI benchmarks. (a, c) Spatial distribution and observation times of the SO_2 pixels used for spatiotemporal matching on (a) June 4 and (c) June 5. (b, d) Scatter plots comparing the bias-corrected GEMS SO_2 total column (scaled by a factor of 0.5) with coincident TROPOMI observations for (b) June 4 and (d) June 5.

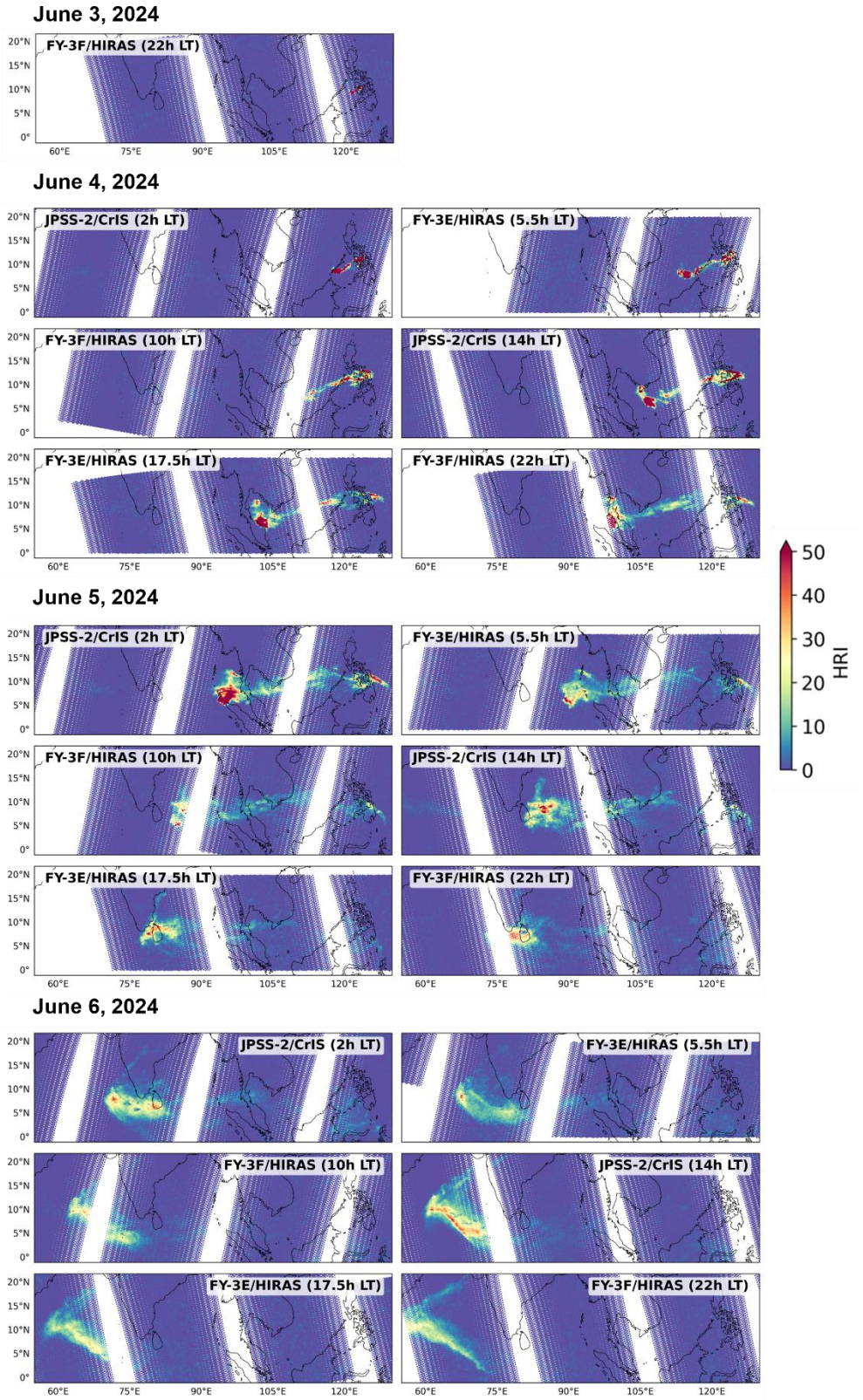

Figure S8. Spatial distribution of the SO_2 HRI derived from FY-3E/F HIRAS and JPSS-2 CrIS during June 3–6, 2024.

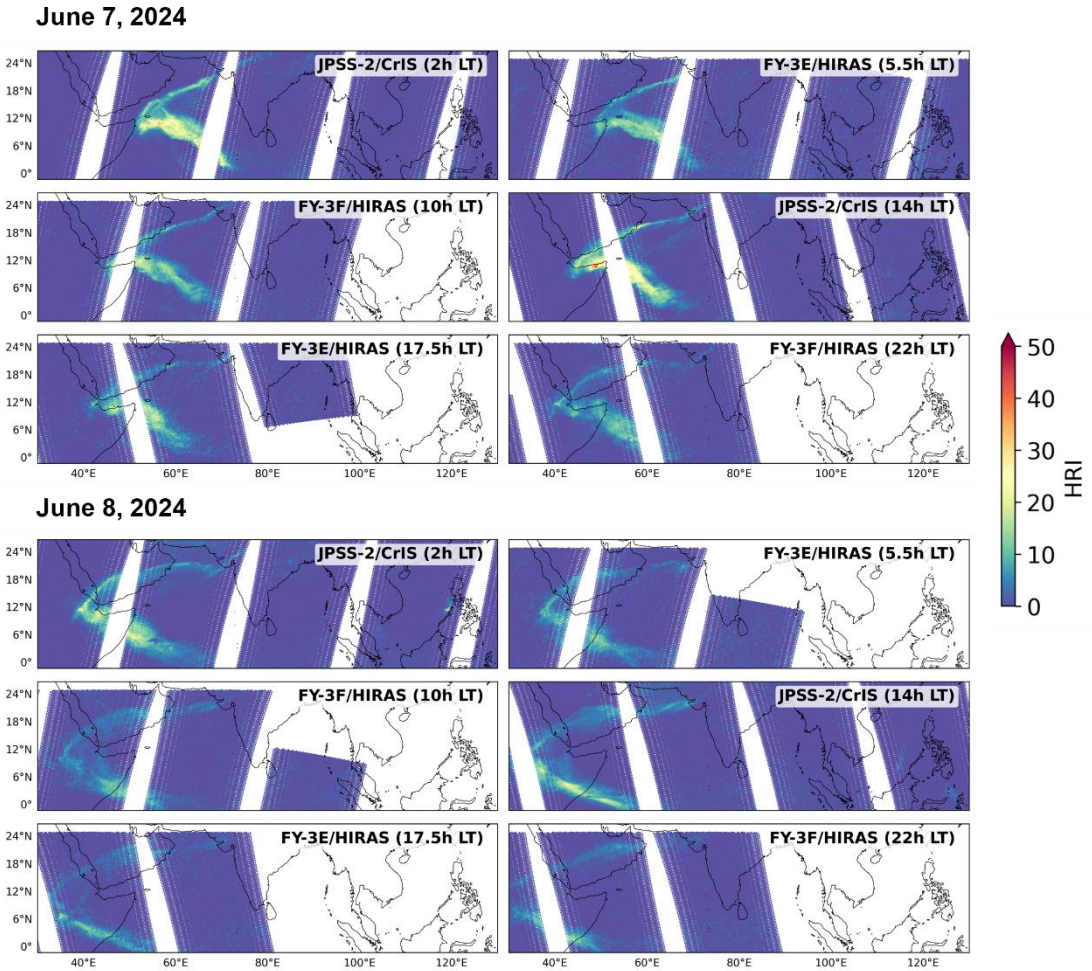

Figure S9. Same as Fig. S8, but for June 7 and 8, 2024.

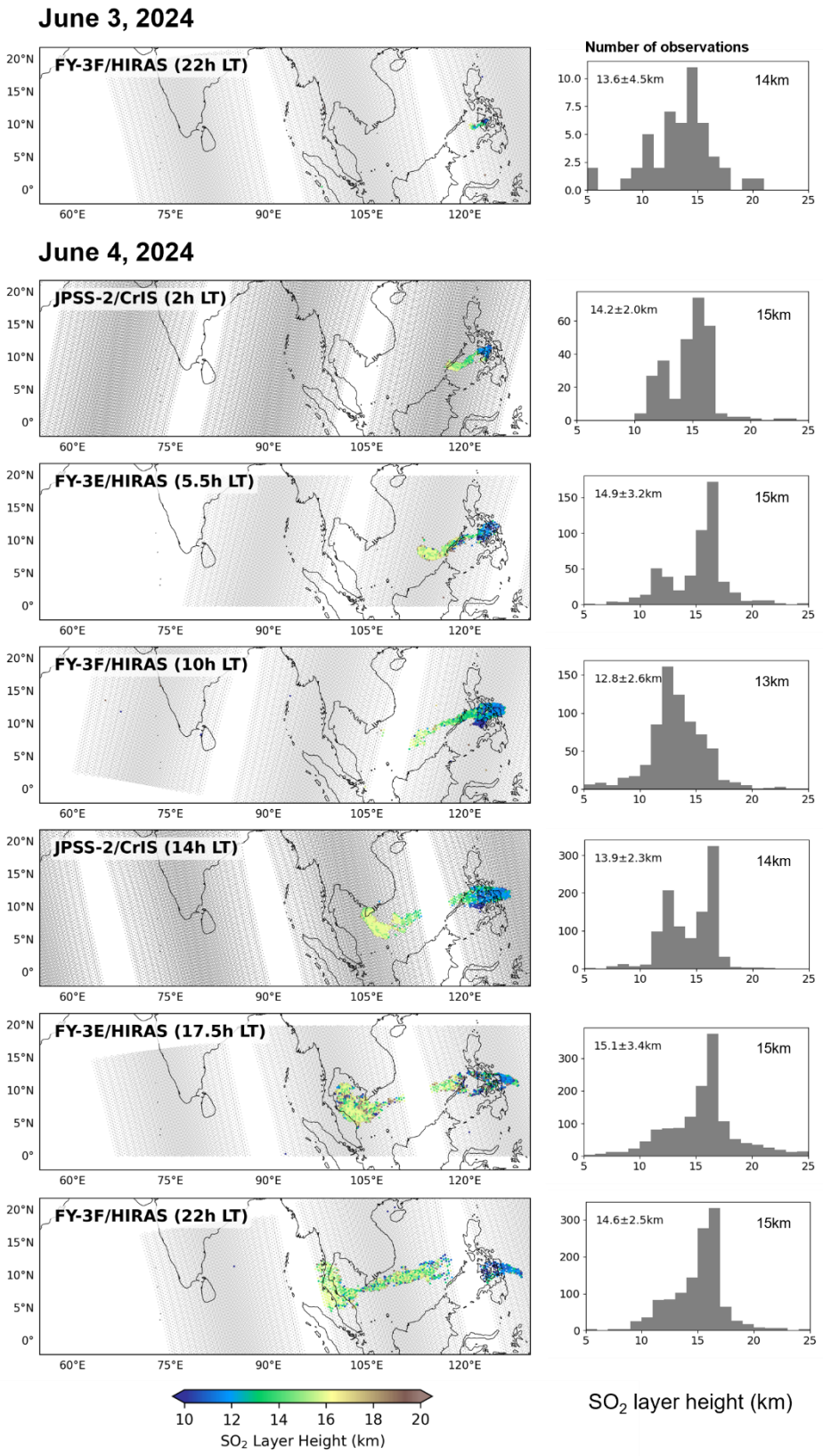

Figure S10. The spatial distribution of the estimated SO_2 layer height and the corresponding histograms for the observations on June 3 and 4, 2024. The inset numbers within each histogram indicate the statistical characteristics of SO_2 height: the values on the left represent the mean ± standard deviation, while the value on the right represents the median.

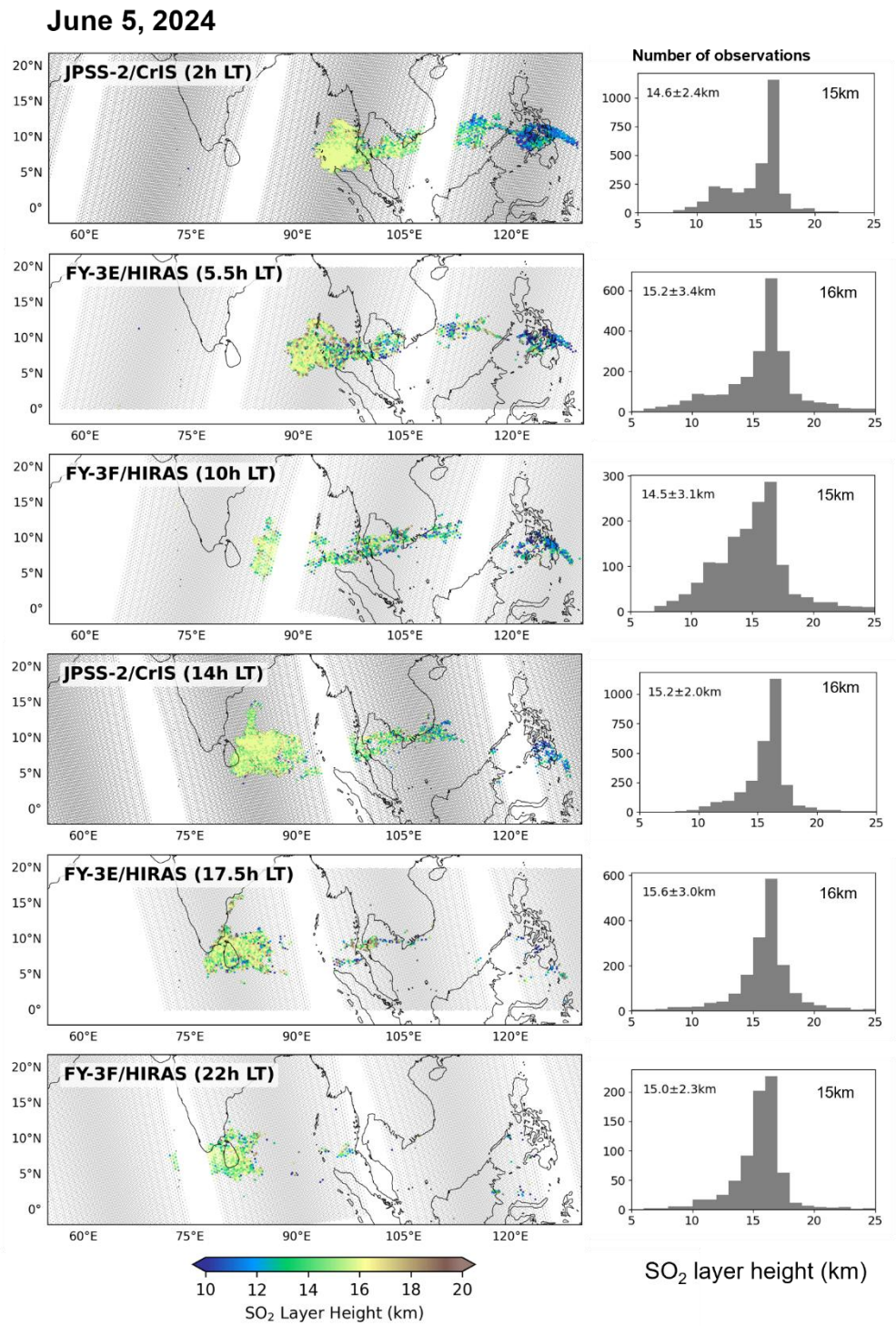

Figure S11. Same as Fig. S10, but for June 5, 2024.

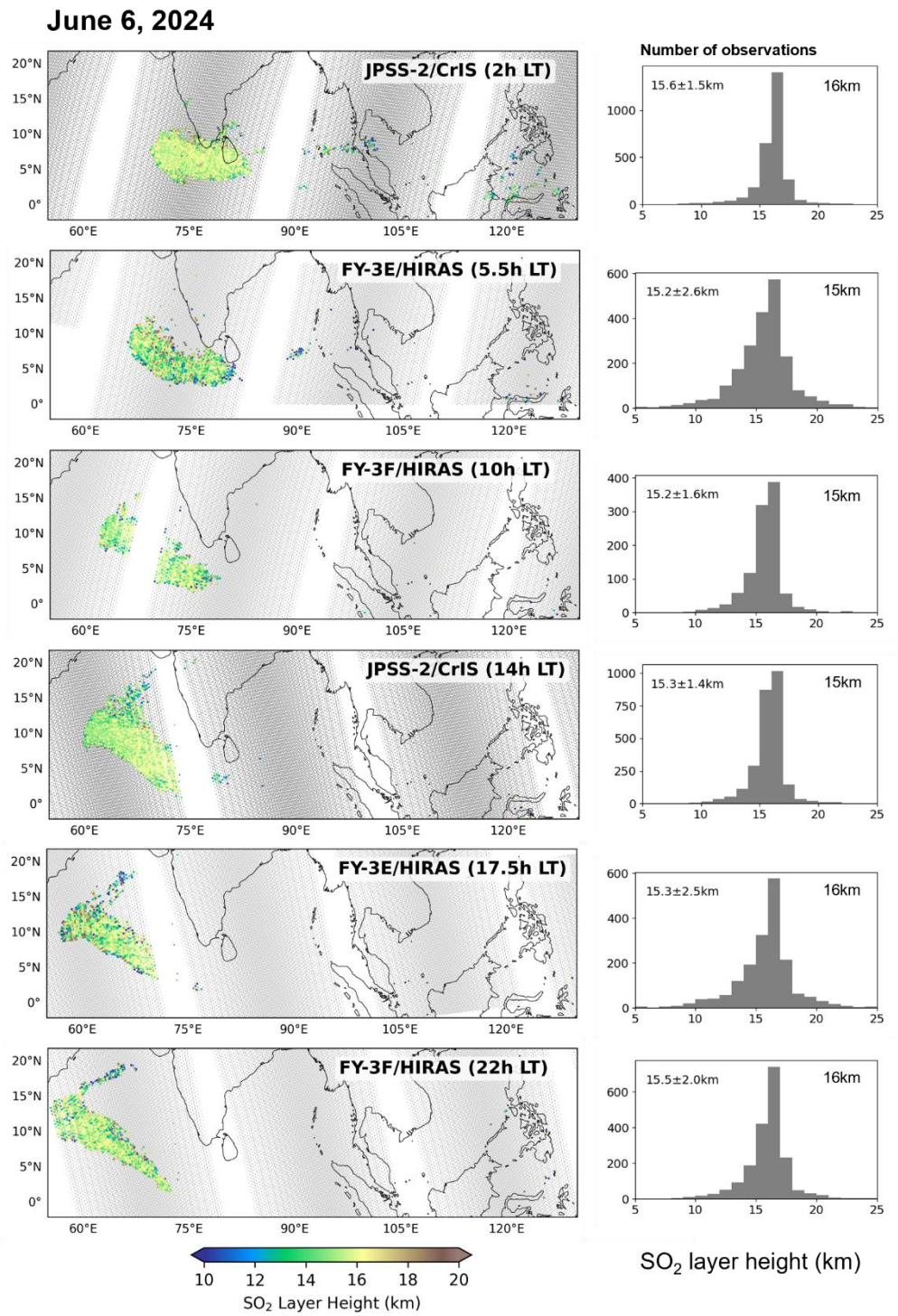

Figure S12. Same as Fig. S10, but for June 6, 2024.

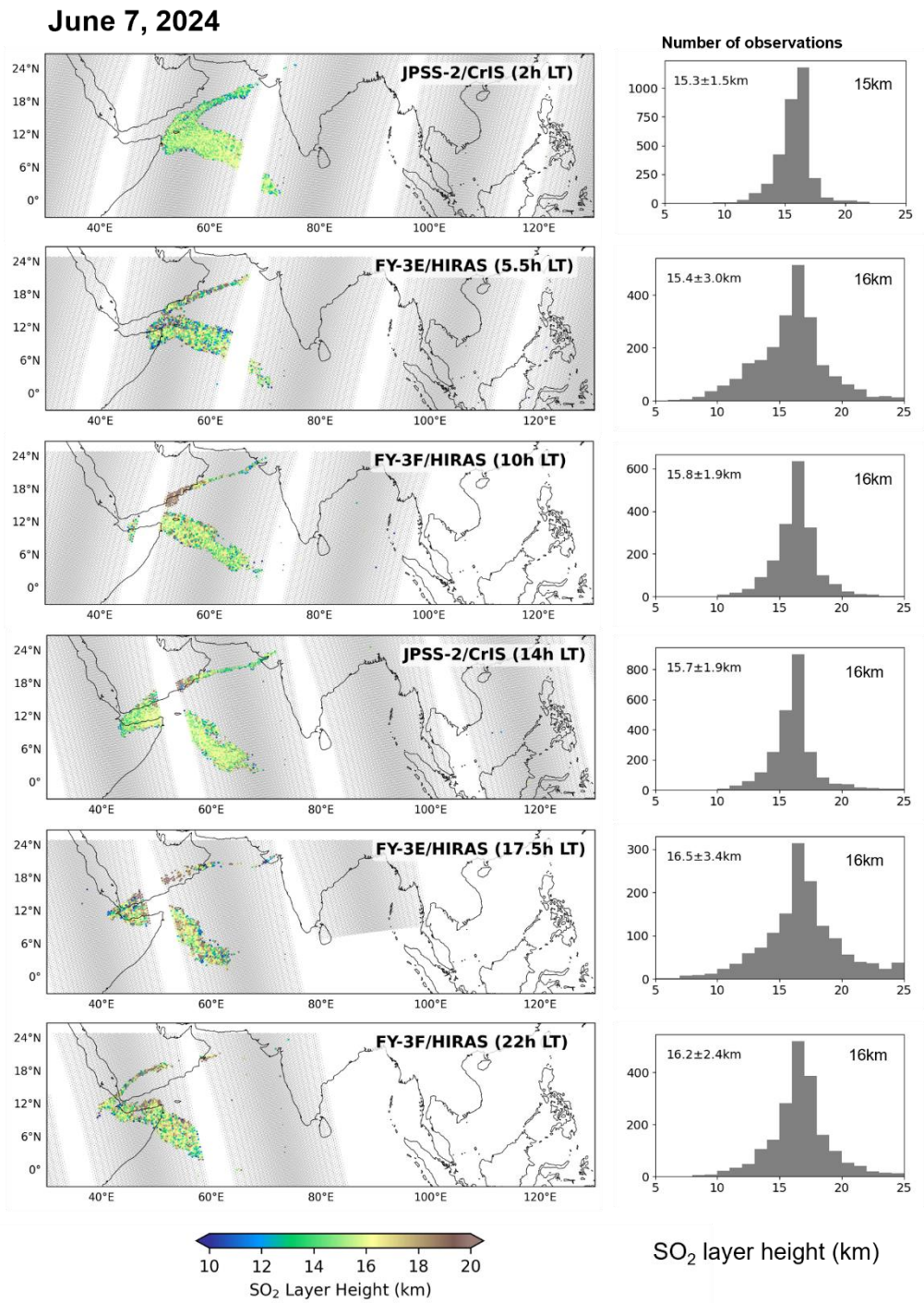

Figure S13. Same as Fig. S10, but for June 7, 2024.

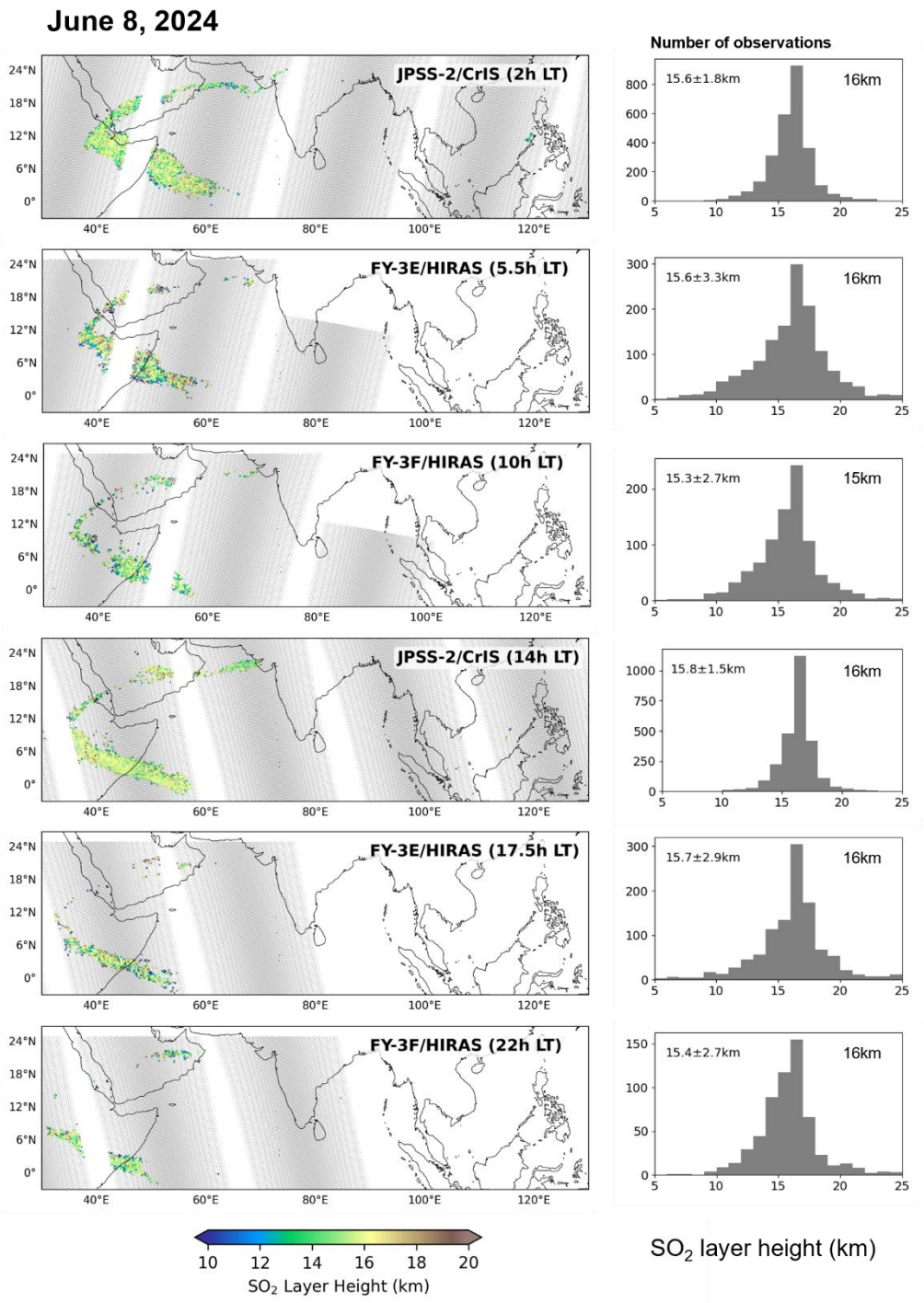

Figure S14. Same as Fig. S10, but for June 8, 2024.

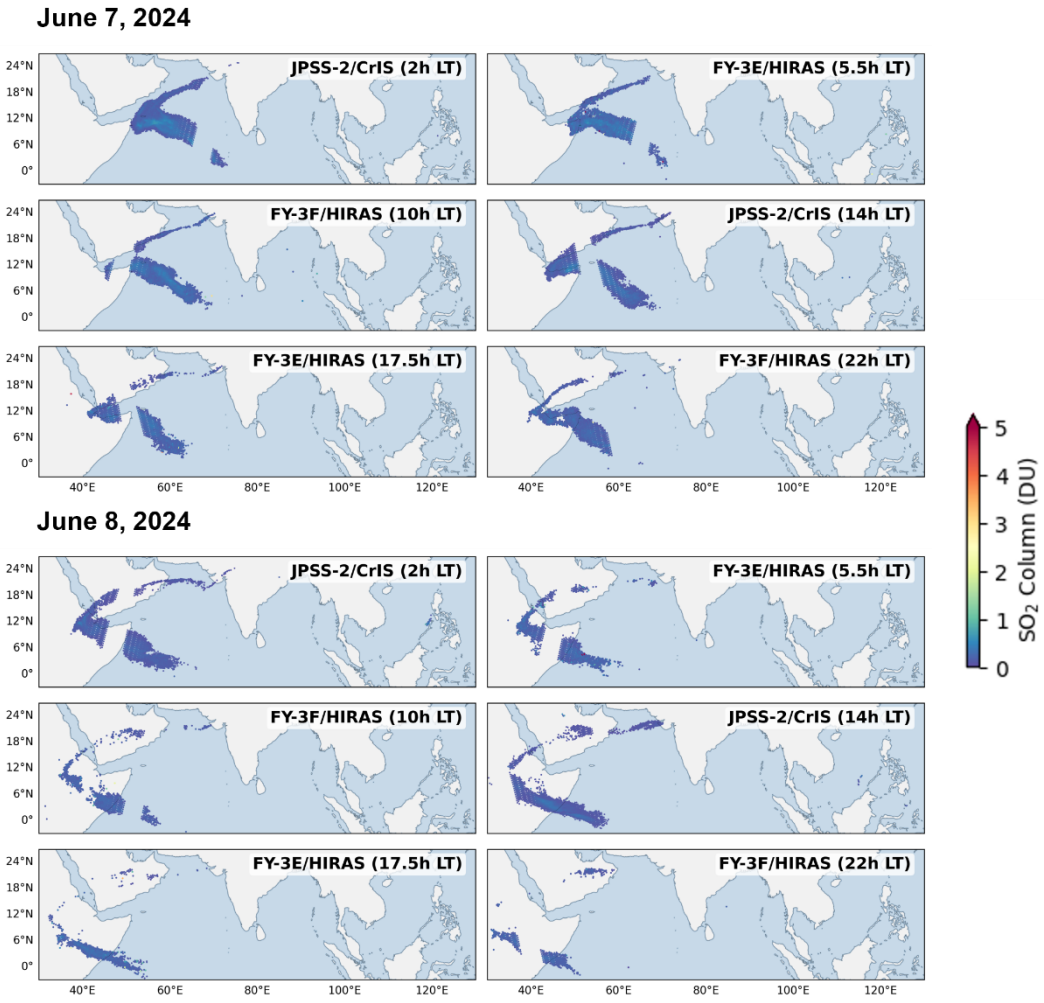

Figure S15. Same as Fig. 7, but for June 7 and 8, 2024.

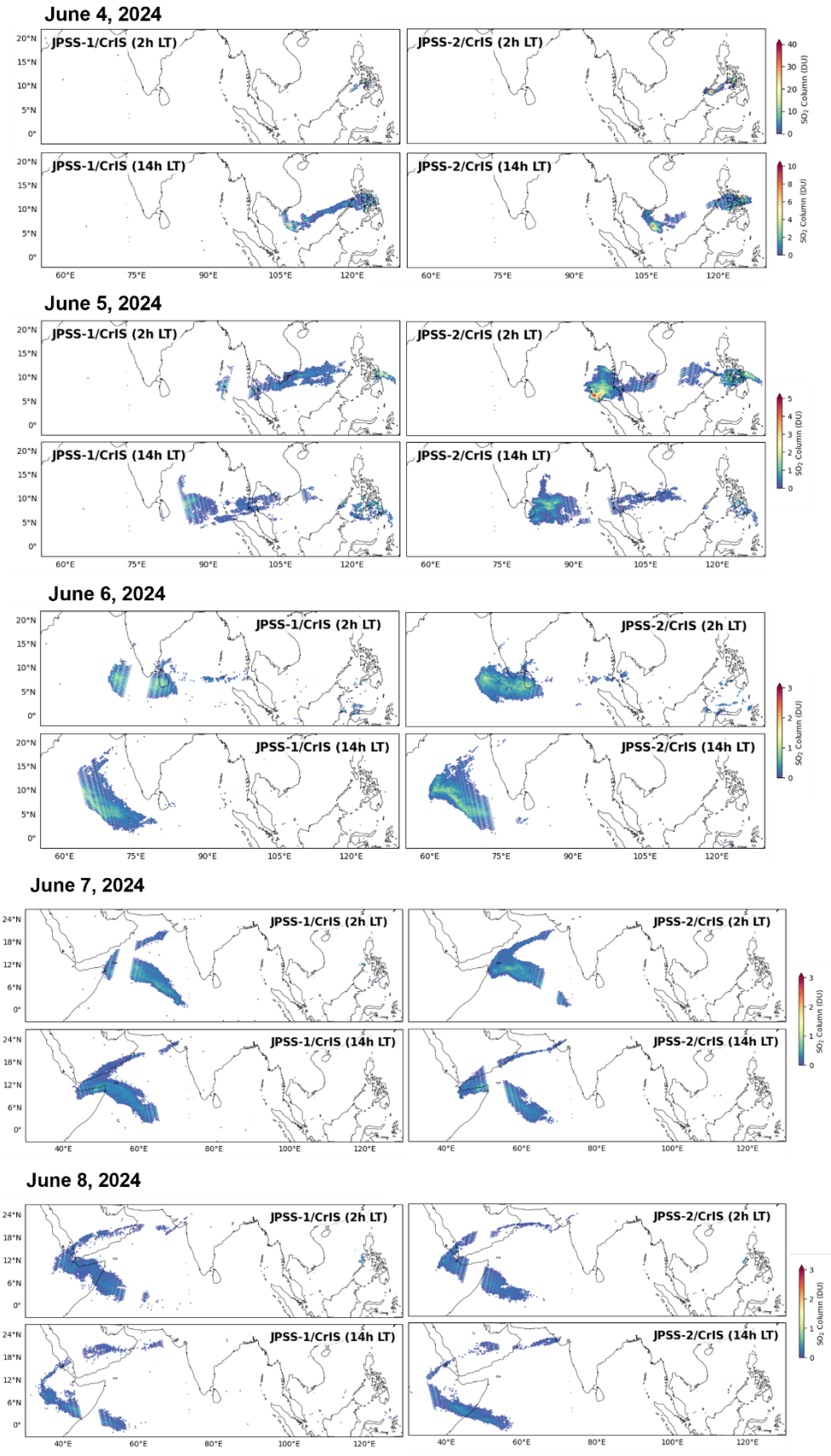

Figure S16. Spatiotemporal evolution of volcanic SO_2 total columns retrieved from JPSS-1/2 CrIS observations during June 4–8, 2024.

(a)

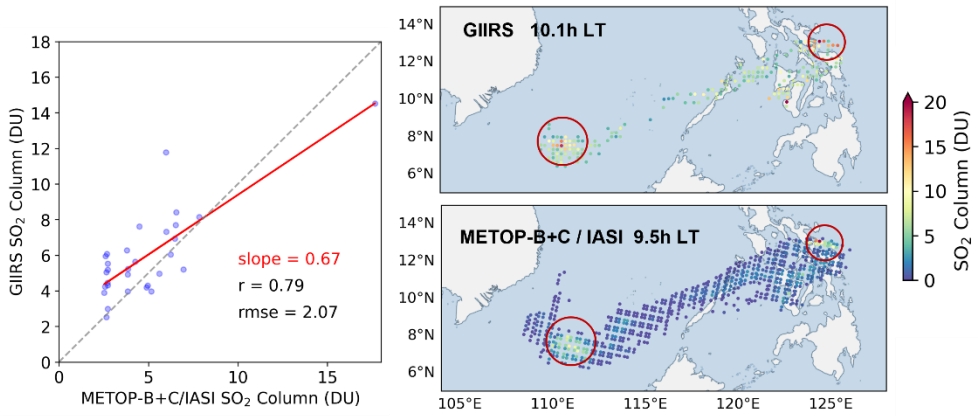

(b)

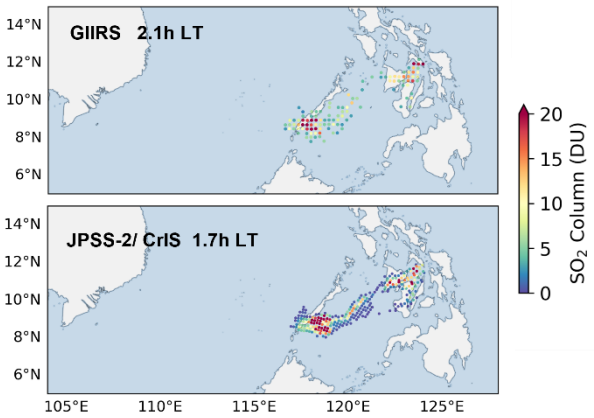

Figure S17. Visual comparison of SO_2 total columns between FY-4B/GIIRS and (a) Metop-B/C IASI, (b) JPSS-2 CrIS. Panels illustrate the consistency in plume morphology, as temporal mismatches preclude direct point-to-point quantitative validation.

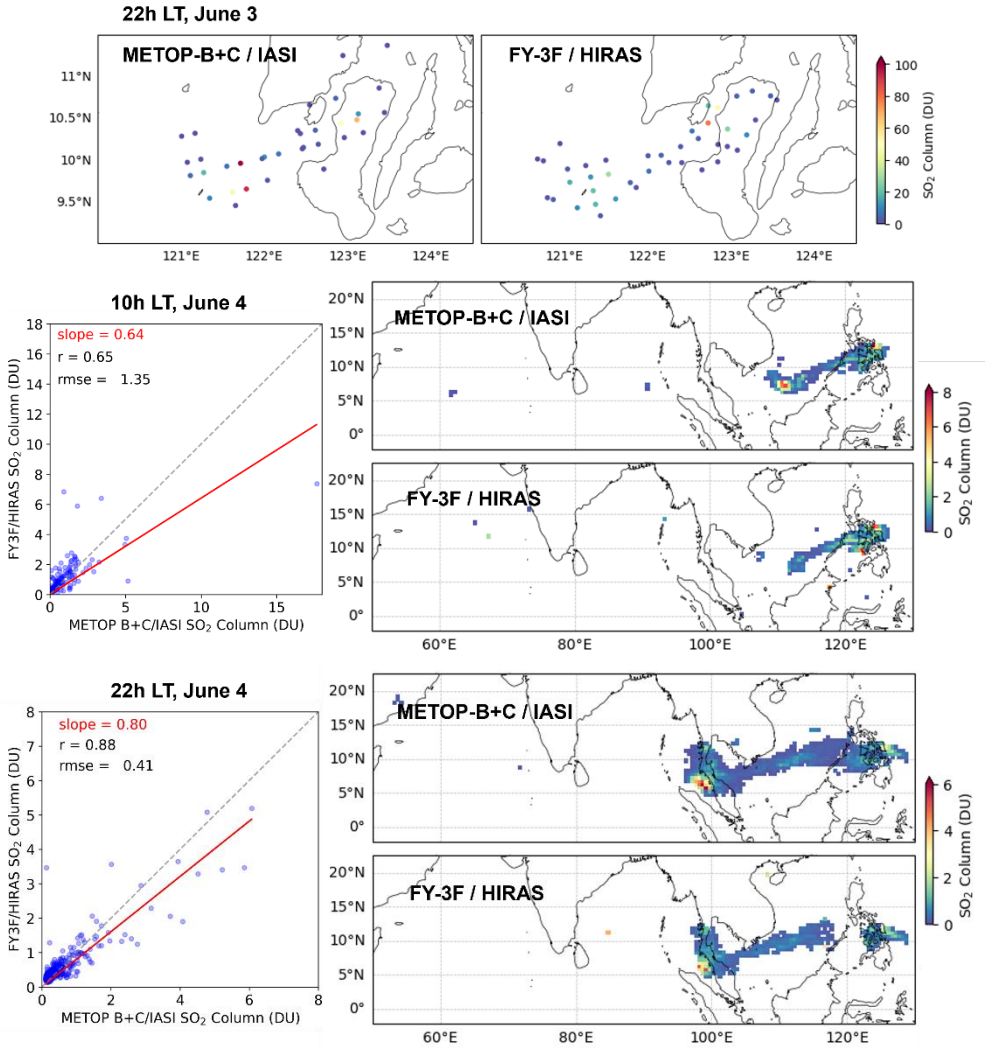

Figure S18. Similar to Fig. 9a but showing additional spatial comparisons of SO_2 total columns between Metop-B/C IASI and FY-3F/HIRAS during June 3–4, 2024.

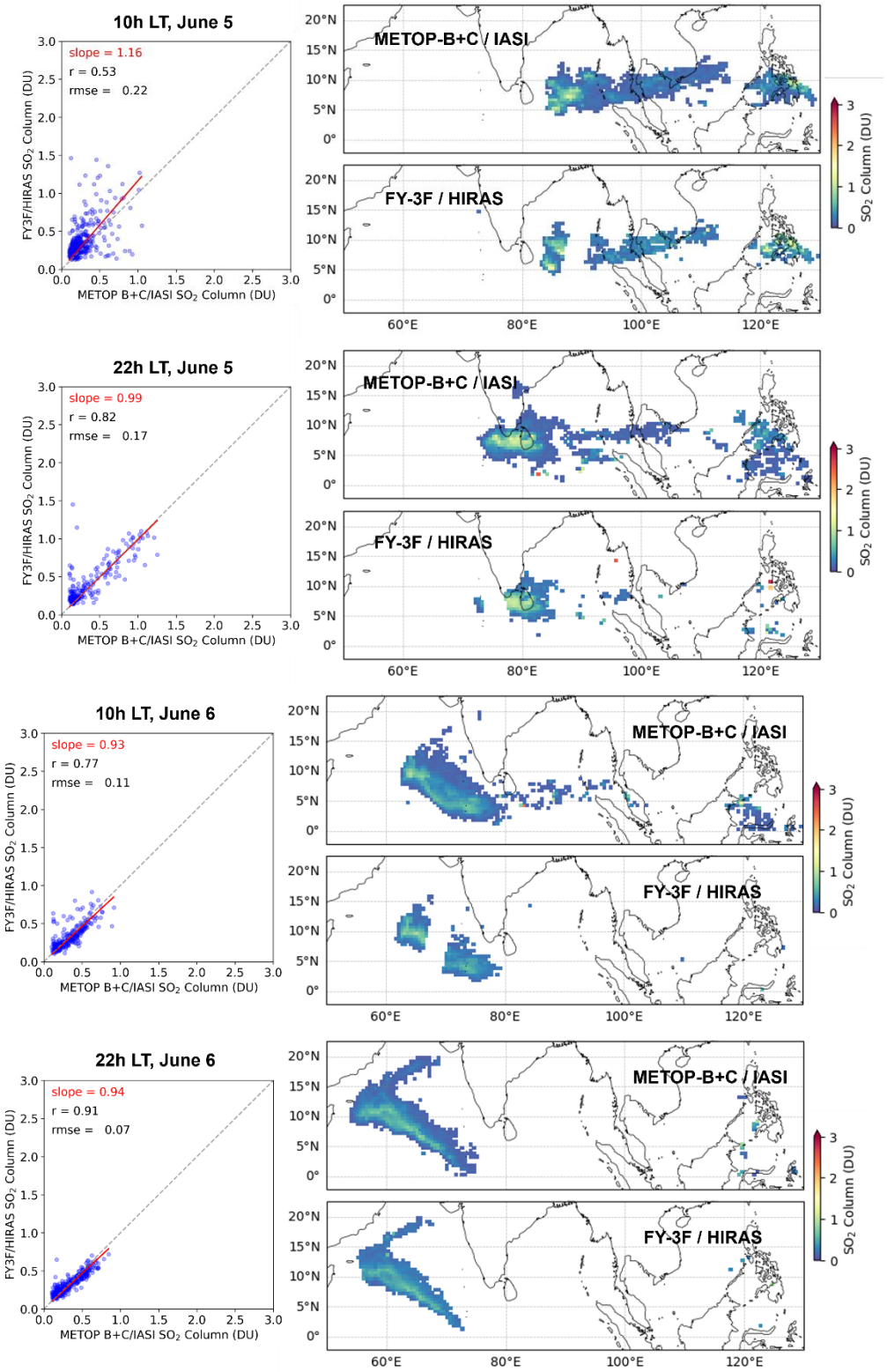

Figure S19. Same as Fig. S18, but for June 5 and 6, 2024.

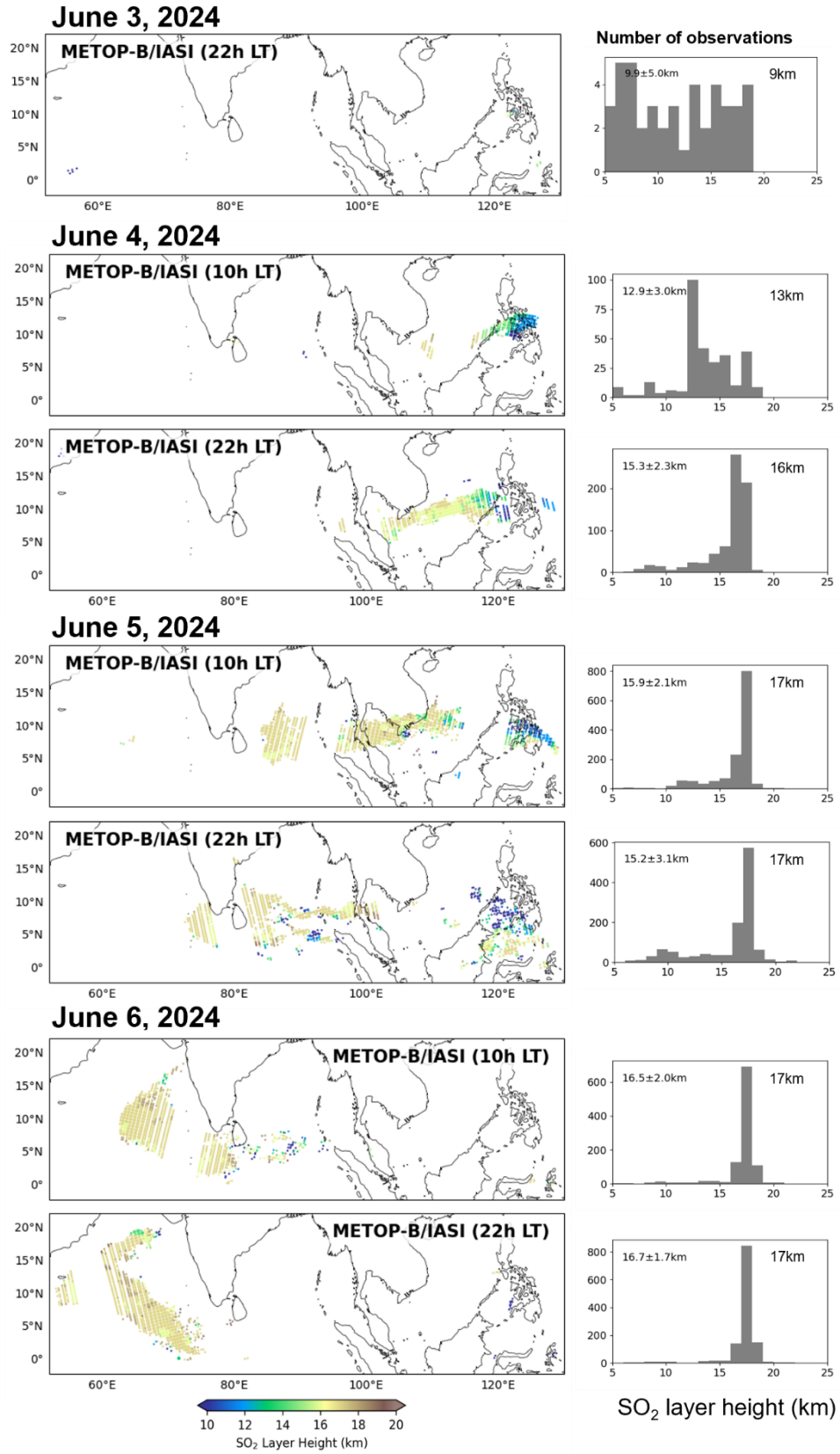

Figure S20. The spatial distribution of the IASI SO_2 plume height and the corresponding histograms for the observations on June 3–6, 2024. The inset numbers within each histogram indicate the statistical characteristics of SO_2 height: the values on the left represent the mean ± standard deviation, while the value on the right represents the median.

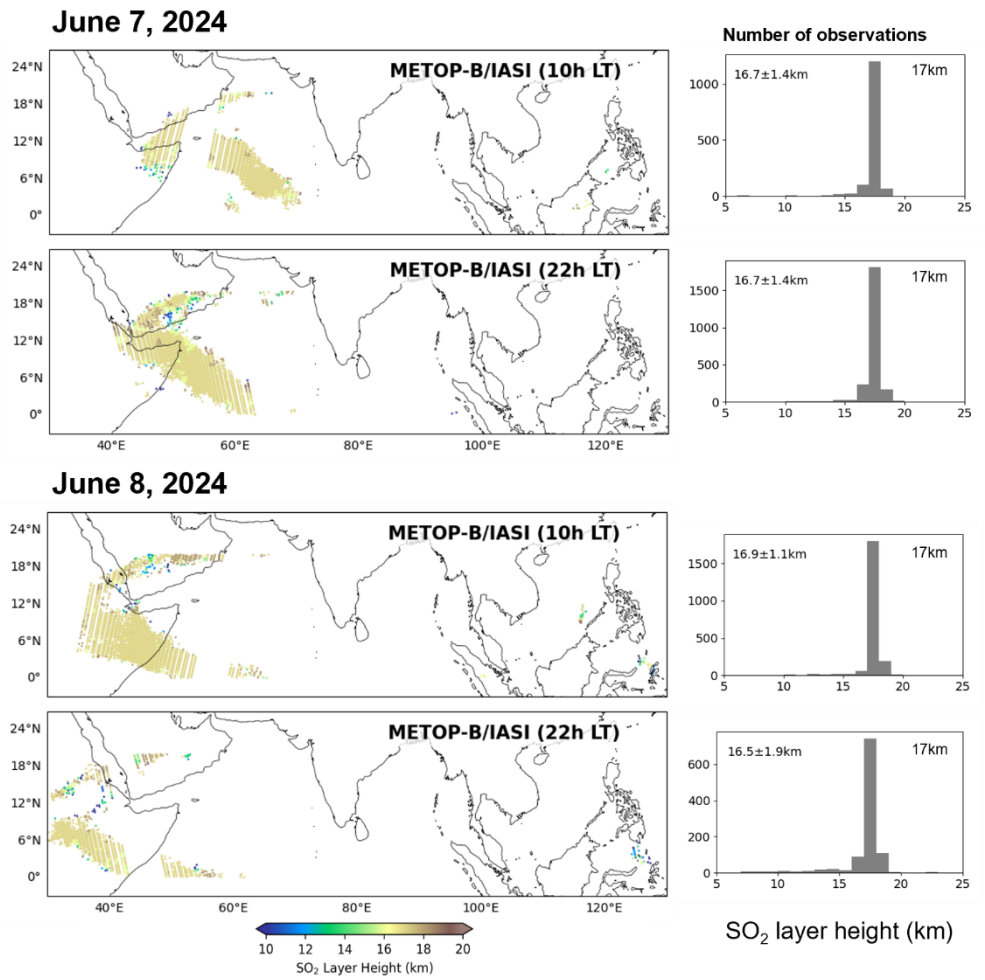

Figure S21. Same as Fig. S20, but for June 7 and 8, 2024.

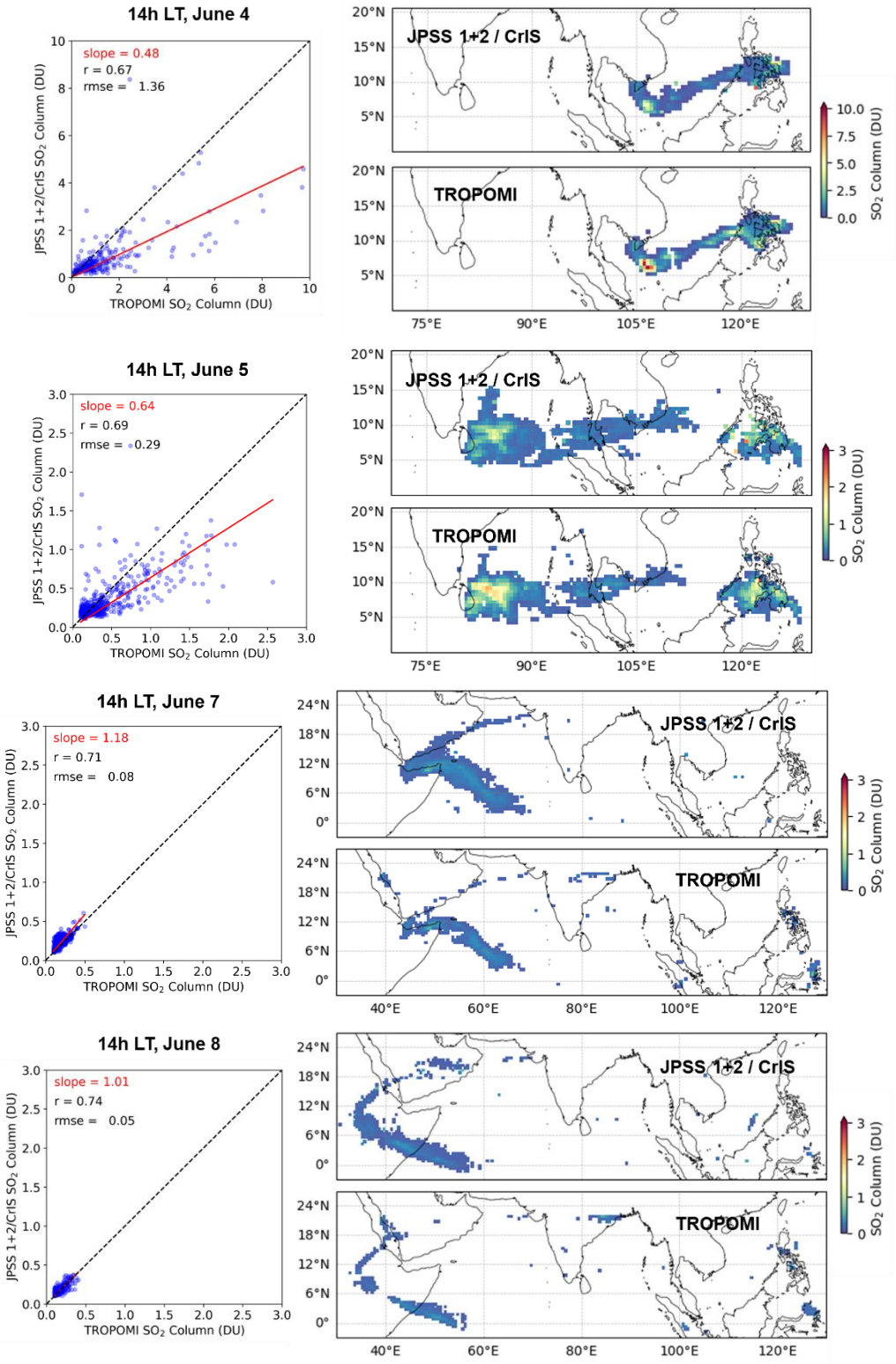

Figure S22. Similar to Fig. 10c but showing additional spatial comparisons of SO_2 total columns between JPSS-1/2 CrIS and TROPOMI during June 4–8, 2024.

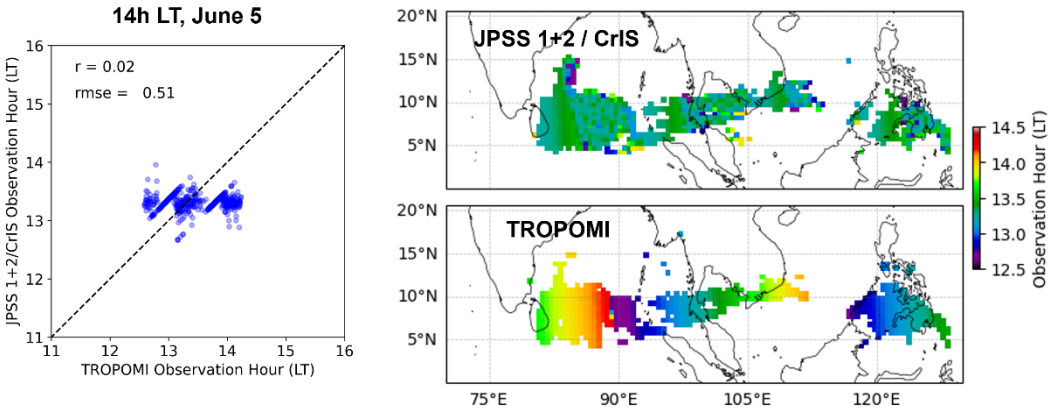

Figure S23. The mismatch of observation time between JPSS-1/2 CrIS and TROPOMI.

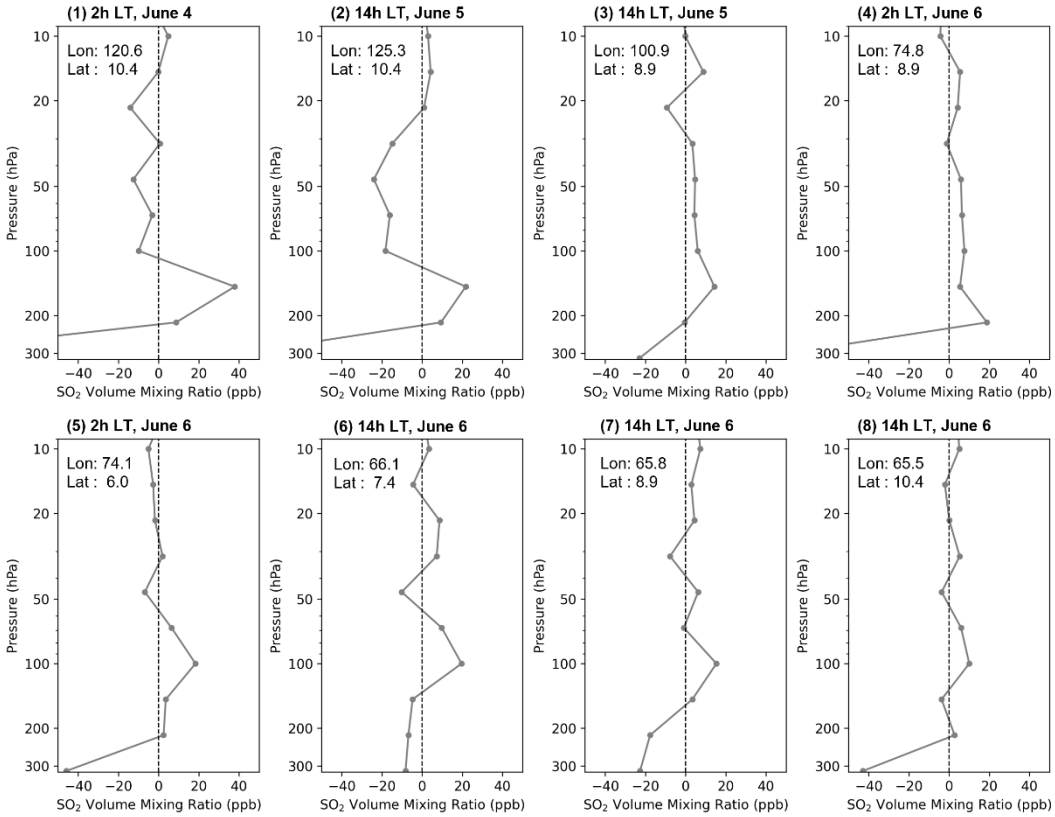

Figure S24. Aura/MLS SO_2 vertical profiles corresponding to the specific footprints marked in Figure 11. Panels (1)–(8) display the vertical distribution of Volume Mixing Ratios (VMR) against pressure for the selected geolocation points. The coordinates (latitude/longitude) and observation times are annotated in each panel.

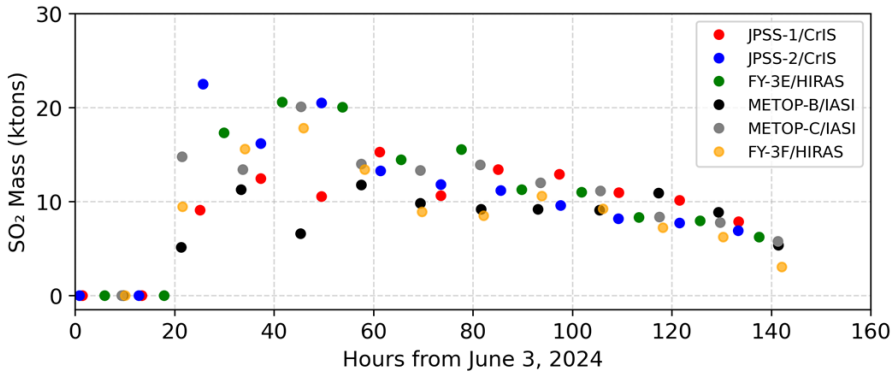

Figure S25. Time series of SO_2 mass loading derived from individual polar-orbiting infrared sensors without spatial gap-filling.

(a)

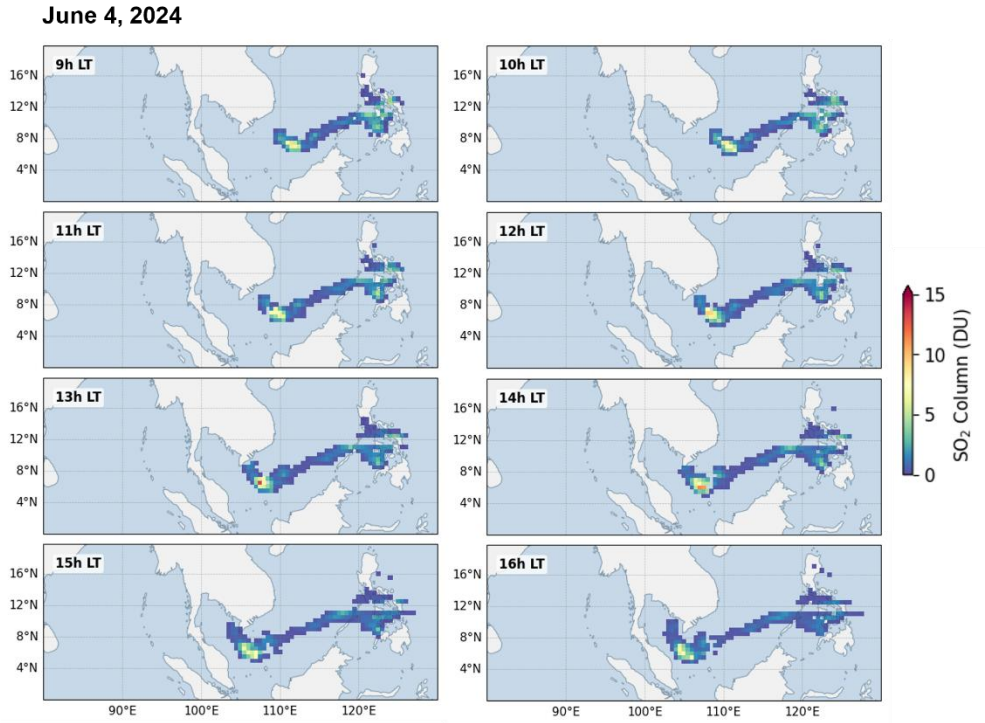

(b)

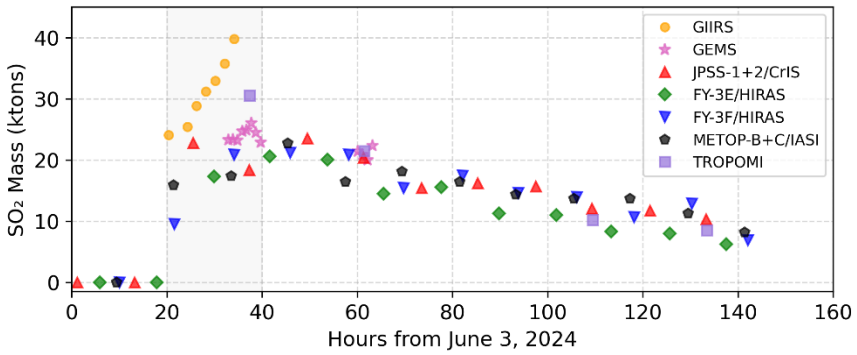

Figure S26. Impact of cloud screening on GEMS SO_2 mass quantification. (a) Similar to Fig. 7 but with a cloud fraction threshold (< 0.7) applied. The resultant spatial discontinuities within the plume indicate the rejection of SO_2-rich pixels mixed with clouds. (b) Time series of SO_2 mass loading derived from the cloud-screened dataset, revealing a systematic underestimation compared to the baseline results (Fig. 12a) due to the compromised spatial integrity.

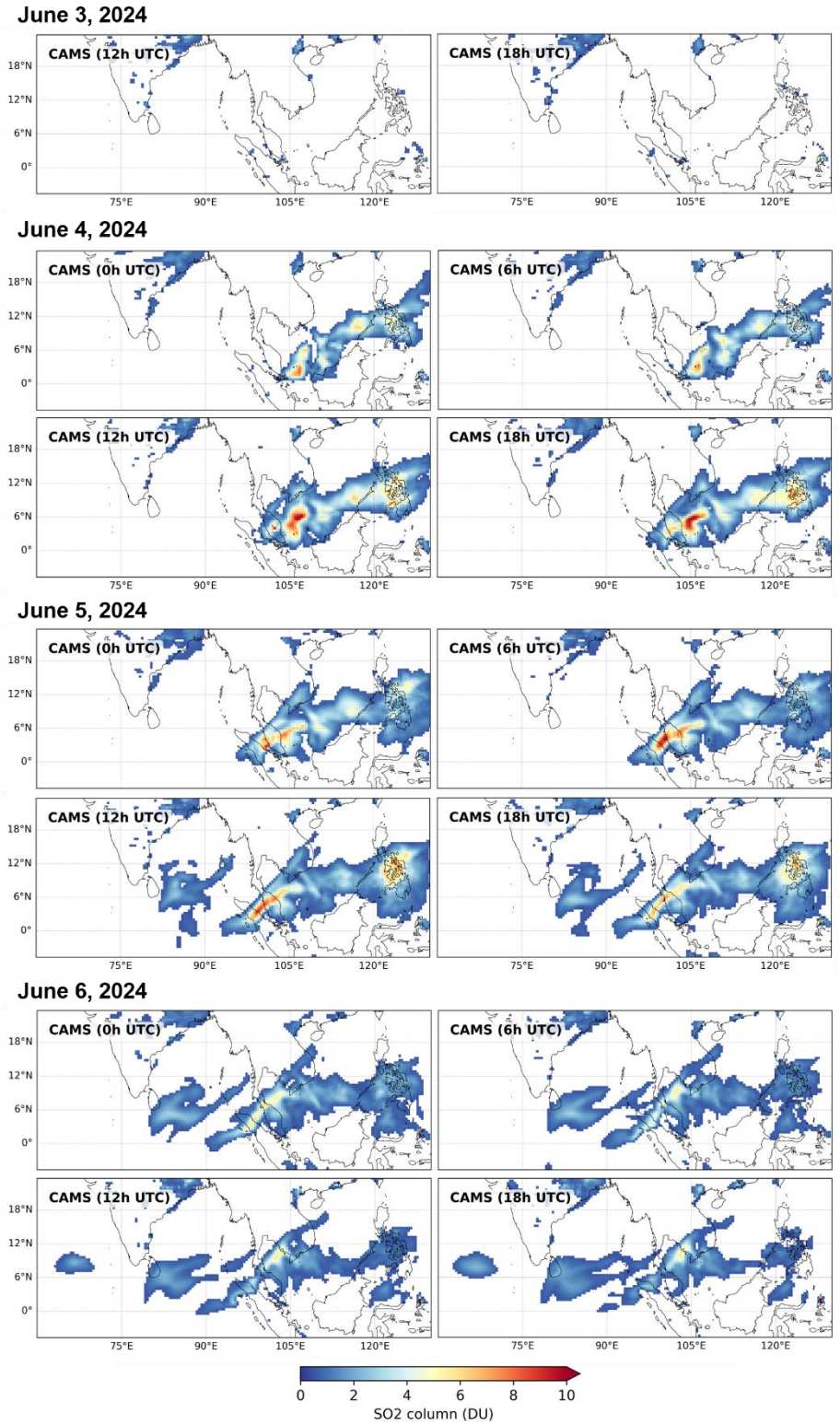

Figure S27. Spatiotemporal evolution of SO_2 total columns simulated by the CAMS forecast model. The panels display model snapshots at 6-hour intervals (00:00, 06:00, 12:00, and 18:00 UTC) from June 3 to June 6, 2024, showing the predicted transport trajectory.

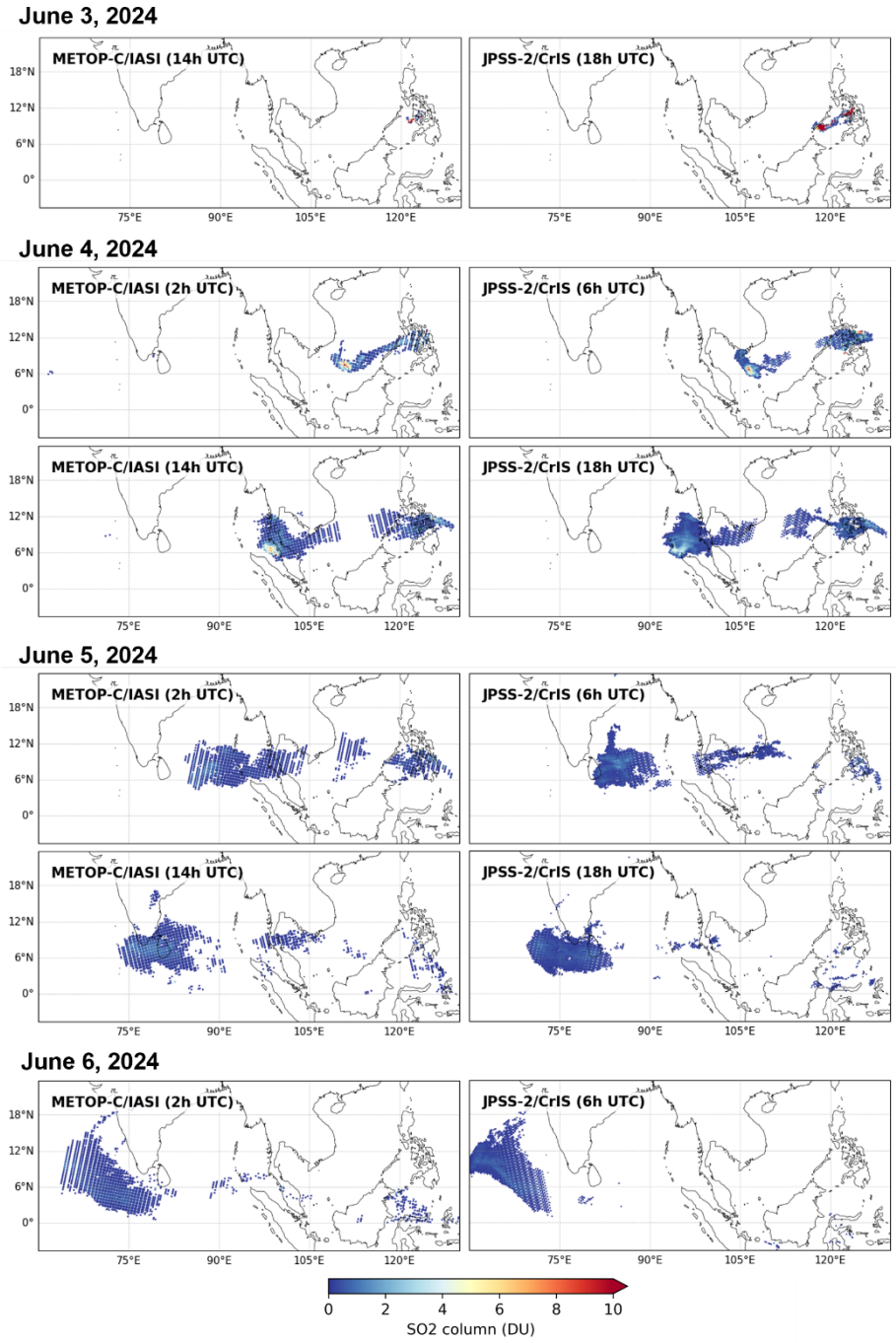

Figure S28. Satellite-observed SO_2 total columns (CrIS and IASI) temporally aligned with CAMS simulations. The observations are selected to match the CAMS output times in Fig. S27 (UTC) to facilitate direct comparison of plume morphology and transport speed.

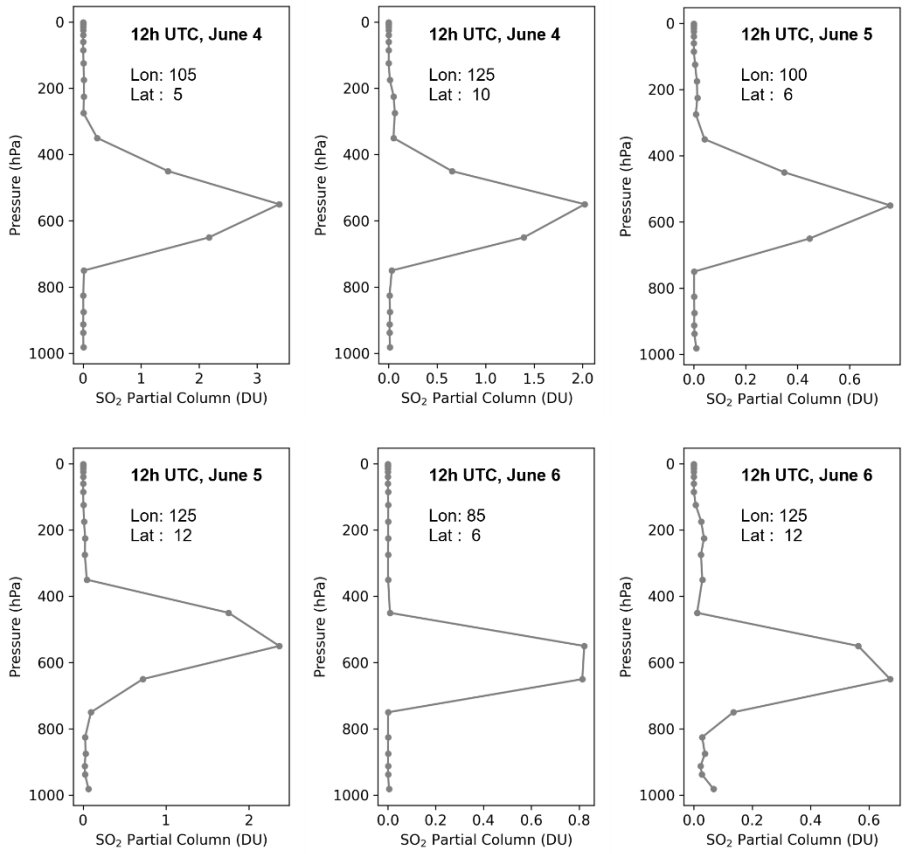

Figure S29. Vertical profiles of SO_2 simulated by the CAMS forecast model at selected spatiotemporal points. The panels display the vertical distribution of SO_2 partial columns against pressure levels for June 4–6 (12:00 UTC).